Materials Research Express

TOPICAL REVIEW

Raman microscopy to characterize plasma-wall interaction materials: from carbon era to metallic walls

C Pardanaud[1,*], C Martin[1], P Roubin[1], G Roussin[1], D Dellasega[2,3], M Passoni[2,3], C Lungu[4], C Porosnicu[4], P Dinca[4], I Bogdanović Radović[5], Z Siketić[5], B Pégourié[6], E Bernard[6], M Diez[6], A Hakola[7] EUROfusion WP PFC contributors[8]

[1] Aix Marseille Université, CNRS, PIIM UMR 7345, 13397, Marseille, France
[2] Dipartimento di Energia, Politecnico di Milano, Milano, Italy
[3] Istituto per la Scienza e Tecnologia dei Plasmi, CNR, via Cozzi 53, 20125 Milan, Italy
[4] National Institute for Laser, Plasma and Radiation Physics, Magurele, Bucharest, Romania
[5] Rudjer Boskovic Institute, P. O. Box 180, 10002 Zagreb, Croatia
[6] CEA, IRFM, F-13108, Saint Paul lez Durance, France
[7] VTT, P. O. Box 1000, 02044 VTT, Finland
[8] See the author list in 'S Brezinsek *et al* 2017 Nucl. Fusion 57 116041'
[*] Author to whom any correspondence should be addressed.

E-mail: cedric.pardanaud@univ-amu.fr

Keywords: Raman microscopy, beryllium, carbon, tungsten, fuel retention

OPEN ACCESS

RECEIVED
28 June 2023

REVISED
20 September 2023

ACCEPTED FOR PUBLICATION
11 October 2023

PUBLISHED
20 October 2023

Abstract

Plasma-wall interaction in magnetic fusion devices is responsible for wall changes and plasma pollution with major safety issues. It is investigated both *in situ* and *ex situ*, especially by realizing large scale dedicated post-mortem campaigns. Selected parts of the walls are extracted and characterized by several techniques. It is important to extract hydrogen isotopes, oxygen or other element content. This is classically done by ion beam analysis and thermal desorption spectroscopy. Raman microscopy is an alternative and complementary technique. The aim of this work is to demonstrate that Raman microscopy is a very sensitive tool. Moreover, if coupled to other techniques and tested on well-controlled reference samples, Raman microscopy can be used efficiently for characterization of wall samples. Present work reviews long experience gained on carbon-based materials demonstrating how Raman microscopy can be related to structural disorder and hydrogen retention, as it is a direct probe of chemical bonds and atomic structure. In particular, we highlight the fact that Raman microscopy can be used to estimate the hydrogen content and bonds to other elements as well as how it evolves under heating. We also present state-of-the-art Raman analyses of beryllium- and tungsten-based materials, and finally, we draw some perspectives regarding boron-based deposits.

1. Introduction

Tungsten (W), beryllium (Be) and carbon (C) based materials are used in nuclear fusion devices as plasma facing components (PFCs). In the past, most of the tokamak PFCs were made of graphite. Its use has been abandoned in 2013 for the ITER tokamak [1] and tokamaks adopting an ITER-Like-Wall configuration [2] because of fuel retention problems extrapolated from existing tokamaks. Tungsten is now chosen due to its good thermomechanical properties (dissipating 10 to 20 MW m^{-2} in steady state operations) and low affinity for hydrogen (H) isotopes [3–5]. Be is used with the aim to trap oxygen (O) impurities by forming oxides [6, 7]. Boron (B) is also envisaged as a complement or instead of Be in order to start discharges efficiently (i.e. conditioning the vessel walls such that the impurity contents could be kept under control) [8, 9]. Because of plasma wall interactions [10], PFC characteristics will be modified during the machine lifetime [11] due to many processes such as erosion, morphological changes, melting, and defect formation [12]. PFCs surface temperature could change drastically, depending on location inside the machine, as the power distribution facing the walls is not homogeneous [13]. The presence of impurities and eroded species that can migrate or

redeposit [14, 15] should also be taken into account. Therefore, the safety conditions of ITER may be compromised, mainly because of the formation of dust [16–18] and the retention of radioactive tritium used to fuel the plasma [19–21]. Materials synthesized in laboratory conditions are used to mimic deposits or modified surfaces [10], such that the fundamental mechanisms behind plasma-wall interaction phenomena could be clarified and predictions for future devices made [22, 23]. Linear plasma devices are also of interest as they deliver intermediate flux between laboratory plasma and tokamaks [24–26]. Post-mortem analyses are also used to obtain a before/after comparison and understand how elements migrate inside the nowadays machines [14, 27–35]. Ion beam analyses [36] and thermal desorption spectroscopy are key techniques that give absolute and relative content. SEM-EDX is also used to reveal element contents, excluding light elements [30]. Confocal, atomic force and electron microscopies give information on the material morphology and porosity, which could be connected to the local properties of the plasma facing the wall [37, 38]. X-ray diffraction (XRD) reveals the structure, crystallite size and gives indirect information of the nature of some hydrogen isotope traps in the material [39, 40]. In addition, spectra obtained by Raman microscopy are based on inelastic light scattering process and therefore very sensitive to chemical bonds, structure and morphology. Raman spectroscopy allows chemical bonds to be identified and, in particular, the presence of defects [41] and surface oxides, that will modify D and T behavior in tokamaks [42], to be detected. Other spectroscopic techniques could be used and are presented in a recent article [43]. The present review discusses the advances made in the field of Raman microscopy of PFCs materials since our 2017 book chapter [44]. It is presented in a way complementary to [43], in order to give a direct access to people not familiar with spectroscopy to see what could be learnt from Raman spectra, and how. We illustrate how powerful Raman microscopy technique could be to convince researchers in fusion related materials to use this technique.

The paper is organized as follows:

- Section 2 presents the basics of Raman microscopy and its relation to the vibrations and chemical bonds of the probed material.
- Section 3 lists what can be derived from Raman microscopy of carbon, beryllium and tungsten based materials. It includes how impurities or defects modify the vibrational signatures, and how important is the choice of the Raman laser wavelength. As carbon leads to very rich vibrational signatures, containing also indirect signatures coming from C-O or C-H bonds. We demonstrate that for beryllium, the problem is similar, forcing one to develop a strategy to detect the presence of oxygen or hydrogen indirectly from the Raman spectra. For tungsten, presence of oxygen leads to a very sensitive signature but finding the hydrogen signature remains challenging.
- In section 4, we discuss a strategy developed in the past for detecting hydrogen and its bonding mechanisms in carbon and how this strategy could be applied in the future for beryllium and tungsten based materials.
- Section 5 discusses opportunities to use Raman microscopy to characterize the nature of boron deposits.
- We give conclusions in section 6.

2. Raman microscopy basics

The general principles of Raman microscopy are summarized in figure 1. The sample to be analyzed is positioned in a XY motorized stage. A laser beam is focused on it through a microscope objective, in a backscattering geometry. The diameter of the probed zone is roughly 1μm and its depth depends on the optical constants. The motorized XY stage allows working in a spectro-imagery mode sensitive to chemical contrasts of the scale of the micrometer. The same objective is used not only to focus the laser beam but also to collect light after beam interacts with the sample. This collected light is a composition of photons from several physical origins: elastically scattered (i.e. Rayleigh scattering), inelastically scattered (i.e. Raman scattering) or photoluminescence photons (i.e. from many possible processes in the material like electron–hole recombination leading to photoluminescence for example). For the inelastically scattered photons, the difference in energy comes from the excitation by the laser beam of vibrational degrees of freedom of the sample, such as stretching or bending motions of atoms, involving collective vibrations called phonons. Two processes exist: the Stokes process that results in energy loss and the anti-Stokes process that results in energy gain (not shown in figure 1). At room temperature, for most of the vibrational energies (in the range $\approx$ 1000–3000 cm^{-1}), the anti-Stokes process is less intense and could be ignored as in general it contains the same information as Stokes process. The quantum mechanical treatment of the interaction generally involves a virtual state, not resonant with an eigenstate of the analyzed material. In the specific case of a resonance, effects (not discussed

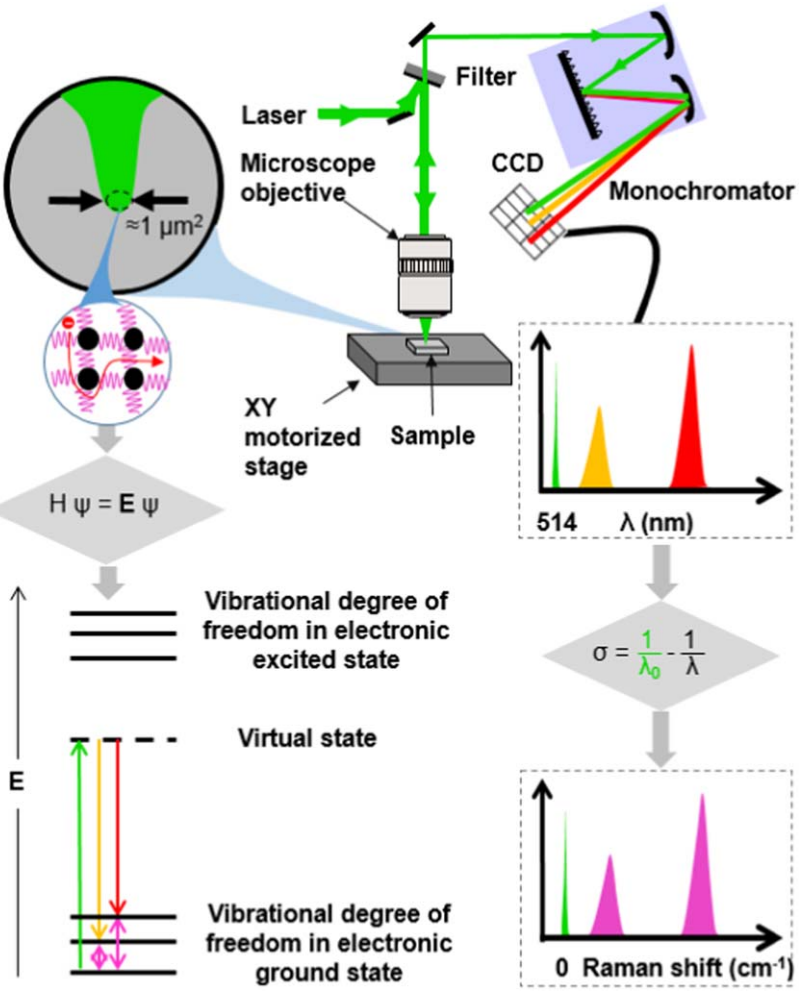

Figure 1. Schematic view of Raman spectroscopy setup used to characterize. Main experimental characteristics, on the top part of the figure, are presented in parallel to the physical effect, described on the left bottom side. In brief: Raman microscopy probes materials, typically 1 μm^2 at a time. Detected photons, in the visible range, contain information related to vibrational energy, which depend from one sample to the other. represents the Raman shift.

here) could modify Raman band intensity and shape. We now focus on the set-up description. As the elastic peak intensity is several orders of magnitude higher than the intensity of inelastic peaks, it has to be filtered out before light could be dispersed and analyzed. A CCD camera records raw data and a spatial calibration of the CCD attributes a wavelength to a camera pixel . As lasers used are in the visible range, the Raman signal is also in the visible range (vibrational energies are in the range 100–3000 cm^{-1} (i.e. 12–370 meV, respectively). To obtain the vibrational energy, the energy of the scattered light is subtracted from the energy of the incident beam: this is called Raman shift (named σ). Raman shifts and vibrational energies are expressed in wavenumbers (in cm^{-1}). The Raman shift for the laser wavelength is thus at 0 cm^{-1} (see figure 1). Note that the intensity of the scattered light behaves like $\approx 1/\lambda^4$, being then more efficient in the blue part of the spectrum. Note that another degree of freedom carrying information is the light polarization. It allows, in principle, to have access to the crystal orientation probed. In this work, we do not exploit polarization because samples are generally micro- or nano-crystalline and poly-oriented, or amorphous.

In figure 2, band intensities of typical samples are compared, and corresponding acquisition conditions discussed. What is presented here is not the Raman cross section, but something more useful for the experimentalists. Band intensities could be intense if cross sections are high or if the number of vibrators under the beam is high (i.e. the laser beam penetrates deeply into the material), or both. Depending on the optical constants, the laser beam penetrates material from a few nm to ≈ 1 μm. The acquisition times reported in figure 2(a) are indicative and vary from one detector to the other. Moreover, one should define the maximum laser power density that can be used in order not to modify the structure of the material by heating. In practice, if the material is not porous and dissipate well the heat given by the laser beam, power density could be increased to increase the signal to noise ratio. In practice, 1mWμm^{-2} is an indicative value and one should take care when

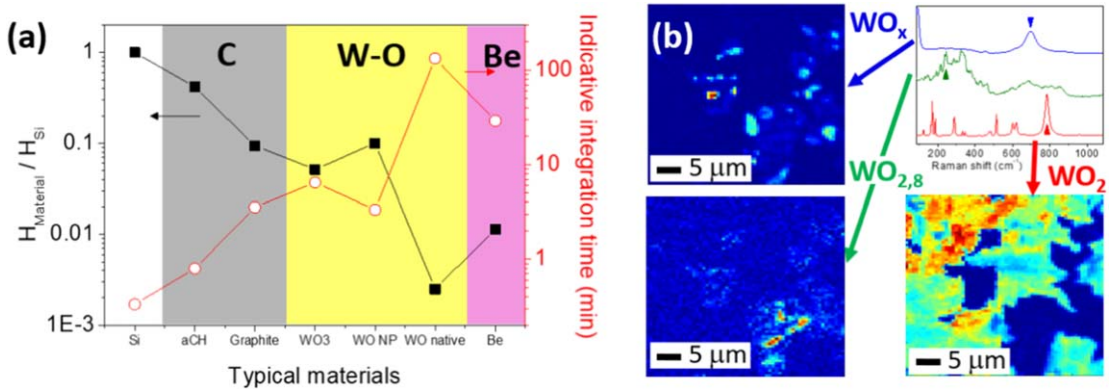

Figure 2. Indicative information concerning data acquisition. (a) Typical band intensity, H, of the main band of the materials of interest (left) and related indicative acquisition time (right). Adapted from [45, 46]. H is the height of the band. Si is silicon, used as a standard material for calibration due to its high intensity. The bands are those at 520, 1582, 800 and 454 cm^{-1}, attributed to Si-Si, C-C, W-O and Be-Be stretching vibrations for crystalline Si, C-based materials, W oxides and Be-based materials, respectively (see below). NP is for nanoparticle. (b) Mapping illustration for heated WO_3, showing the spatial distribution of $WO_{2.8}$, WO_2 and WO_x. Laser wavelength used for this figure is 514 nm.

being close to this value (illustration of this could be find in [45]). In figure 2(a), the acquisition times are given for this indicative power density value (note that they are proportional to one over this power density: if the power density is 0.1 mWμm^{-2}, acquisition times will be multiplied by 10 for a similar signal to noise ratio). Silicon, a reference sample used for calibration, gives one of the most intense Raman bands. Note that remarkably, the intensity of the bands of amorphous hydrogenated carbons (200 nm thick on silicon) is of the same order of magnitude (see [46] for more information about the influence of the thickness and optical constants). Spectra with sufficient statistics could be obtained in a minute or less for these samples. Graphite is found to result in 10 times less intense bands than silicon, but exploitable spectra could be obtained within minutes. For tungsten trioxide and powders of oxide nanoparticles, the situation is similar to graphite, but very sensitive to the thickness of the oxide layer (see [45]). Native oxide layers are more difficult to probe as it requires roughly 100 min to obtain spectra. Beryllium is intermediate: a spectrum with a good signal to noise ratio could be obtained in 20 min. All these collection times remain under 100 min, which does not take much time. One might conclude that it is easy to get data quickly using Raman microscopy. This is only true if the samples are chemically homogeneous. For chemically heterogeneous samples, multiple spectra need to be recorded making measurements more time consuming. Depending on the sample area that needs to be analyzed as well as beam lateral resolution, acquisition times could be increased by two to three orders of magnitude. Figure 2(b) gives the example of a WO_3 sample heated at 750 °C in argon atmosphere for one hour. Raman spectra and maps presented in figure 2(b) were recorded at room temperature in air, after heating. Its thickness is close or below 2 μm (i.e. as thick as the depth zone that probed by the Raman microscope). All together 4440 spectra were collected, each spectrum in 10 seconds, to obtain 44 × 54 μm^2 map in nearly 12 h. Three different chemical environments have been found: WO_x, x being unknown, $WO_{2.8}$ and WO_2. The intensities of the relevant bands (found at 700 cm^{-1} for WO_x; at 240 cm^{-1} for $WO_{2.8}$ and at 790 cm^{-1} for WO_2) are plotted on the same area giving lateral distribution of three chemical environments. Although scale bar is not shown, the relative abundancies could be deduced from the relative intensity ratios if the sample thickness and the optical constants are well known. An example is given here for thick sample with a high Raman cross section so that in one overnight acquisition, a large zone with a 0.75 μm step can be probed. For thinner samples and/or samples with less intense Raman signal, a compromise has to be made to obtain similar maps, with a good signal to noise ratio either by reducing the size of the zone probed or reducing the step or by increasing the time acquisition.

3. Raman spectroscopy of C, Be and W based materials

We now focus on carbon, beryllium and tungsten based materials which are the most important materials for PFC in fusion related devices. Figures 3, 4 and 5 show the typical Raman spectra of carbon, beryllium and tungsten oxide, respectively (tungsten alone is not Raman active). Figures 3(a)–5(a) display typical spectra of these materials with different phases or with different amounts of structural disorder or with different stoichiometry in order to show the variety of spectral shapes and give an idea of the possibilities for quick identification. Figures 3(b)–5(b) display Raman spectra of one selected sample but recorded using different laser

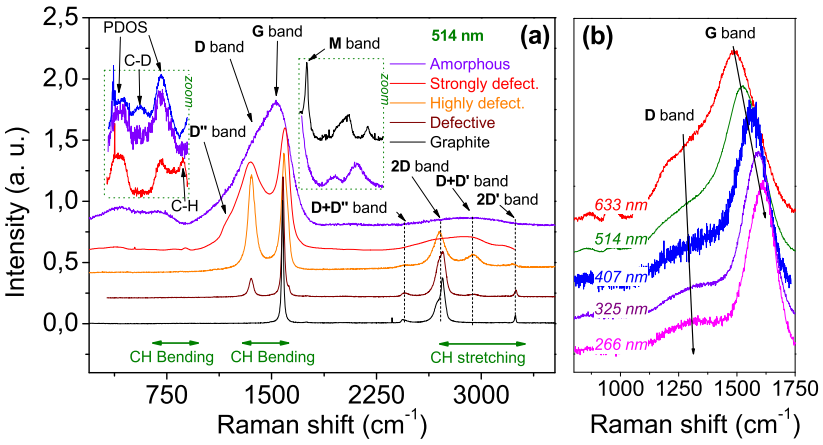

Figure 3. Typical Raman spectra of disordered and amorphous carbons. (a) Using 514 nm laser beam. (b) Using various laser wavelengths in the case of amorphous carbons. Data are taken from [47, 48].

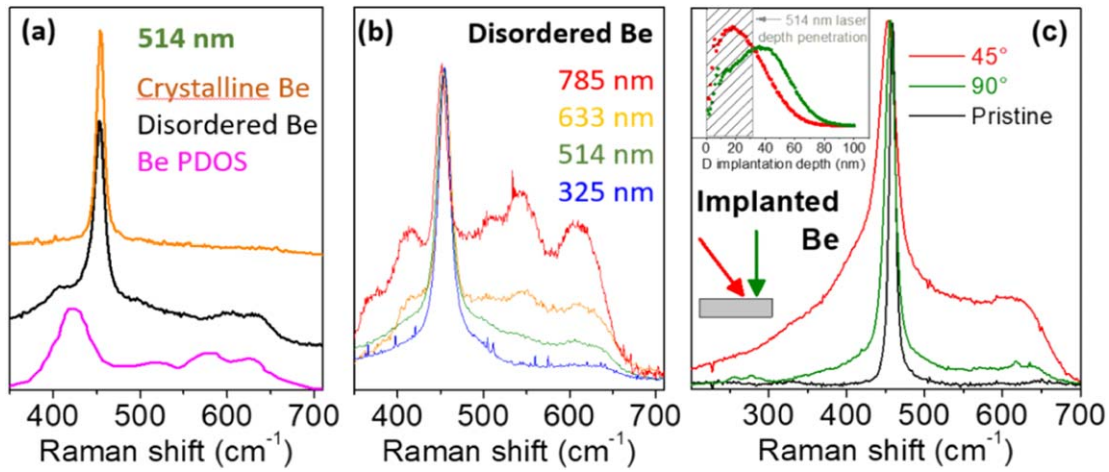

Figure 4. Typical Raman spectra of crystalline and disordered beryllium. (a) Using a 514 nm laser. (b) Using various laser wavelengths. (c) 2 keV D ions implanting Be under 2 different implantation angles. Data are from [44, 49], except 785 nm data which is original.

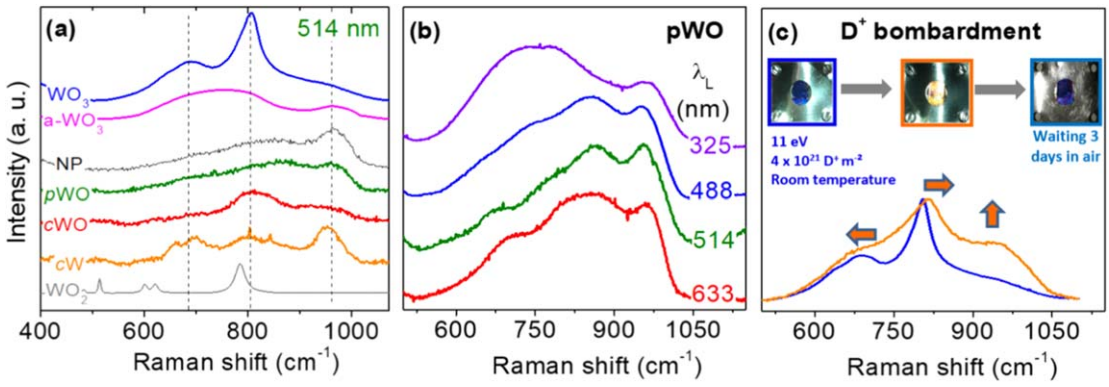

Figure 5. Typical Raman spectra of tungsten oxides. (a) Using 514 nm laser. (b) Using various laser wavelengths for a porous tungsten suboxide. (c) Implantation of 11 eV D^+ and reversible effect by storing the sample in air for 3 days. Data of figure (a) are from [45] and references there in. Data of figure (c) are adapted from [50]. Data of figure (b) are original data.

wavelengths. This should highlight the fact that care should be taken when using a single laser wavelength or when trying to compare data acquired with another laser wavelength. First C, then Be and W based materials will be discussed. A separate section is devoted to Be oxides and hydrides. Finally, several plots of relevant spectroscopic parameters, useful to deduce the level of defects in the sample, are presented.

3.1. Raman spectroscopy of carbon materials

Figure 3(a) displays Raman spectra of different aromatic based carbons, from highly oriented pyrolytic graphite to amorphous carbons, which mainly contain sp^2 bonds. Discussion on diamond, nanotube, or fullerene structures is excluded from this overview. More general review is given in [47]. Pyrolytic graphite is composed of well-stacked graphene planes. Structural disorder can exist either in the plane, or perpendicular to it. Raman spectroscopy gives insight to these two kinds of disorder. Graphite belongs to the $P6_3/mmc$ (D^4_{6h}) space group [51] and exhibits only a limited number of Raman active modes. The most intense band related to those modes belongs to a E_{2g} representation, lying at 1582 cm^{-1}, the so-called 'G band'. Other bands, related to the way graphene layers are stacked, could be found below 125 cm^{-1} [52], but they are not necessarily intense and depending on the experimental set-up, could fall too close to the laser wavenumber to be measured. Due to an electron–phonon coupling interaction [53], and an electronic resonance mechanism (called the double resonance mechanism), other bands could appear in the spectrum of sp^2 based carbons. The most intense of these bands, called the 2D band, lies at 2720 cm^{-1} using a 514 nm laser. Its intensity is roughly 1/3 of the G band intensity and is composed of some subcomponents for pyrolytic graphite. For monolayer graphene and graphite in which stacking in the perpendicular direction is disordered, this band has a Lorentzian shape [54, 55] and can vary in intensity. For amorphous carbon, the intensity compared to that of the G band falls down to a few %. Another important band, as we will see later, is the D band lying at 1350 cm^{-1}. This band is related mainly to the in-plane defects. Also related to defects, a D' band exists near 1615 cm^{-1}, sometimes overlapping with the G band. For samples with many defects (grain sizes in the nanometric range), a D' band is present in the red shoulder of the D band. Several weaker bands, like the M band, are also present in the 1500–2500 cm^{-1} region. Most of them are described in [56] for graphite. The physical origin of those bands is reviewed in [47]. Note that there are some combination of bands, such as D+D' and D+D', in the 2000–3000 cm^{-1} region. The presence of disorder modifies their relative intensities. The position, widths and relative intensities of bands can change with the laser wavelength, as displayed in figure 3(b). This is mainly due to the resonance effects and to the aromatic domain size distribution. It is worth mentioning that the dispersion of some bands could be used to better characterize defectivity, see [47, 55] and references therein.

The carbon skeleton, built networks of sp^2 and sp^3 bonds, and that leads to all above mentioned bands totally hides signatures coming from the other chemical bonds. Indeed, C = C bonds lead to very intense bands due to resonance mechanisms enhancing the Raman cross section. C-O or C-H related bands, that fall in the same range of frequencies, are much less intense and therefore totally hidden. C-D related bands fall in between these carbon bands but are still partially hidden. For carbon, only one weak band related to a C–H bond is reported at 860 cm^{-1}, falling close to two broad bands related to the phonon density of states (PDOS) [57], also coming from carbon skeleton, and that rises in the case of amorphous materials [58, 59]. Due to an isotopic effect, this band redshifts at 550 cm^{-1} when D substitutes H. We have also detected C-D bands in Be+C samples with a large amount of D [60] which will be discussed below. This is covered in more details when discussing figure 6. In conclusion, Raman spectra of carbons could be used very efficiently to evaluate the sample defectivity (see figures 7(a) and 8). On the other hand, to evaluate hydrogen content from Raman spectra, indirect way should be taken as illustrated in figures 9 and 10.

3.2. Raman spectroscopy of beryllium

Figure 4 displays Raman spectra of crystalline and defective beryllium samples. Figure 4(a) compares a crystalline and a defective sample (recorded with a 514 nm laser beam). One Raman active mode is observed for crystalline Be, belonging to the E_{2g} representation. The corresponding band, allowed by quantum selection rules and crystal symmetry, lies at 450 cm^{-1}. Its width is close to 7 cm^{-1}. Four broad extra bands appear for disordered samples. These bands are not allowed by quantum selection rules and crystal symmetry. They are identified as being due to the PDOS of beryllium and appear because of presence of defects [49]. Comparing the PDOS intensity to the Raman allowed band intensity allows obtaining qualitative information on the crystallinity of the material (figure 8 will refer to this point). Figure 4(b) presents the influence of the laser wavelength on the Raman spectrum shape of a disordered sample. Clearly, the ratio of the PDOS intensity to that of the E_{2G} band increases with the wavelength. Intensity changes with the wavelength. Those changes are not of the same nature as for carbon. Here, the dominant effect is that the intensity of the Raman allowed band follows the $1/\lambda^4$ dependency whereas the PDOS does not. During ion bombardment, defects are created inhomogeneously in depths, due to the collision cascades. The laser itself could penetrate at a depth different than the size of the collision cascade.

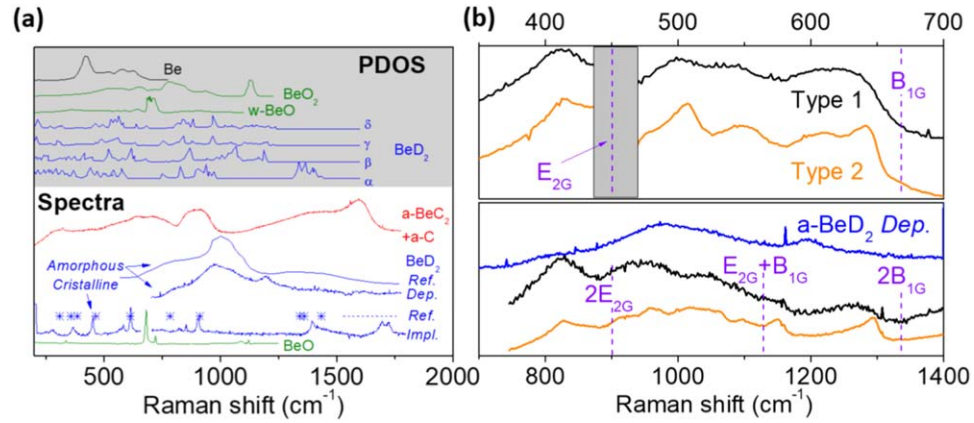

Figure 6. Beryllium carbide, oxide and deuteride. (a) Raman spectra and theoretical PDOS comparison [61–67]. (b) focus on the Be PDOS spectral region (top) and its overtone (bottom). Ref - spectrum from literature, Dep - deposited, Impl - implanted. Data of figure (a) are from many sources cited in the text. Data of figure (b) are from [49, 68].

Two lasers penetrates at different wavelength (of the order of few tens of nanometers in the visible range). Then, it is possible to obtain two different spectra using two different wavelengths for a same collision cascade. This could lead to underestimate amount of defects. In figure 4(c), it can be seen that two samples bombarded by 2 keV D ions at two different angles (45° and 90°) lead to two very different Raman spectra, showing a much more intense PDOS (i.e. the existence of more defects) in the case of 45°. This is because: (1) the laser probe depth is ~30 nm and (2) deuterium implantation depth is ~20 nm for 45° geometry and ~40 nm for 90° geometry. Thus, to concentrate on a region close to the surface, shortest possible wavelength is to be used.

3.3. Raman spectroscopy of tungsten oxides

Crystalline tungsten is not Raman active. Its PDOS (composed of two broad bands, not shown) is found below 300 cm^{-1} [83]. Nitrogen inclusions have been shown to activate this PDOS [45], and the presence of other defects is suspected to activate it as well. However, what can be detected efficiently and unambiguously by Raman microscopy is the presence of tungsten oxides. Tungsten oxide building units are WO_6 octahedra: 1 tungsten and 4 surrounding oxygen form a basal plane, and 2 out of plane oxygen, above and below that plane, form the octahedra. This is at the origin of bands lying close to 270, 714 and 805 cm^{-1}. These octahedra are corner- or edge-sharing to form the numerous tungsten oxide polymorphs observed in the nature. Spatial arrangement of octahedra ~~are~~ controll~~ing~~ stoichiometry, interatomic distances, and symmetry. Several WO_3 phases exist [84] depending on the temperature and the nanostructure size [41, 75]. Stoichiometries close to trioxide, and so-called Magneli phases, have been reported earlier [85]. Independently of the stoichiometry, the spectra are mainly composed of bands related to bending (100–300 cm^{-1}) and stretching modes (700–800 cm^{-1}) of W-O-W bonds, in addition to a band related to the vicinity of the surface (≈950 cm^{-1}) [75, 86, 87]. Figure 5 shows Raman spectra of some tungsten oxides. Synthesis and spectra of Pulsed Layer Deposits (PLD) (compact or porous texture, corresponding to cWO and pWO, respectively), crystalline and amorphous (WO_3 and a-WO_3, respectively), nanoparticles core–shell structures (NP), native tungsten oxide (cW) or WO_2 have been discussed in more details in [45]. The main conclusions of such studies are [88, 89]: (1) compact and porous films lead to Raman spectra that are distinguishable and (2) spectra of porous films and oxides found on W nanoparticles are similar, displaying a mode related to the surface bonds, lying at 960 cm^{-1}. Spectra of a typical porous WO sample, recorded with 4 different laser wavelengths are collected in figure 5(b). The spectra are similar in the red to blue laser but exhibit changes when approaching the optical gap value, close to 4 eV. Figure 5(c) displays the influence of a D bombardment (11 eV, 4×10^{21} $D^+.m^{-2}$ at room temperature, see [50] for more details) on a WO_3 layer. A change in the sample color has been correlated to the formation of tungsten bronze (D_xWO_{3-y}). No direct evidence for O-D or W-D bonds has been found. However, D trapping at low incident energy has modified band shift, position as well as width, which is an indirect consequence of the presence of D. Storing the sample in the air for 3 days has revealed a change back, both in color and in the Raman spectrum, showing that D left the layer.

3.4. Raman spectroscopy of beryllium carbides, hydrides and oxides

The search for vibrational spectroscopic signatures of Be-D or Be-O bonds is a challenging task as can be seen from figure 6. Phonon density of states increases with the defect amount in the material. For carbon, the PDOS signature is mainly hidden because of resonance bands and cannot be used easily, which is not the case for Be for

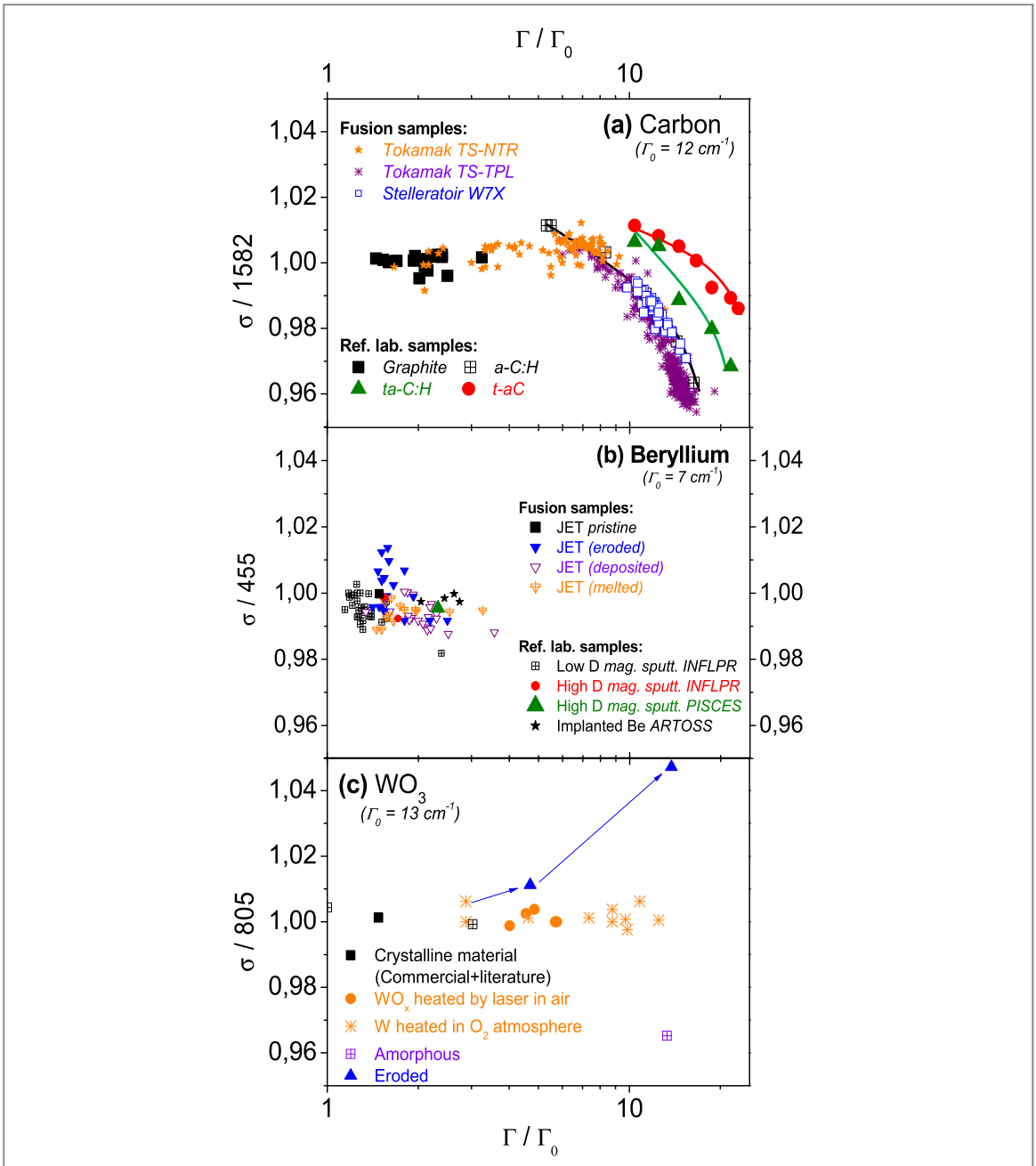

Figure 7. Band position as a function of the band width for a wide variety of samples (reference samples and magnetic fusion devices). (a) Carbon [31, 44, 47, 69–72]. (b) Beryllium [49, 68, 73, 74]. (c) Tungsten oxides [50, 75]. This kind of plot allows to capture quickly both nature and dispersion of samples, detecting big differences in different location of a nuclear fusion device, for example. Laser wavelength used is 514 nm here.

which there is no such resonance. Up to now, in addition to the Raman allowed band at 450 cm^{-1} and the PDOS in the range 300–700 cm^{-1}, all the spectra recorded on Be in air [49, 68, 73, 90, 91] display two extra signatures: a broad signature which roughly displays the same shape as the PDOS but at the double wavenumbers, and a few structured sharp bands. Both broad and sharp signatures fall in the range 700–1300 cm^{-1}. We have previously named the broad signature 2PDOS as we thought it behaved like the PDOS harmonic, and the sharp signatures were named $2E_{2G}$, $E_{2G}+B_{1G}$ and $2B_{1G}$ as they fall close to the second harmonic and combination of Raman allowed E_{2G} and Raman forbidden B_{1G} modes. Other combinations are theoretically possible, but would require single-crystalline samples to be investigated. The area under the 2PDOS curve is in general found to be between 0.1 and 1 compared to PDOS but can be up to 3 times larger in some cases [68]. The area related to the $2E_{2G}$, $E_{2G}+B_{1G}$ and $2B_{1G}$ sharp related signatures are weak. Disorder in the material may affect the shape of all these signatures. For example, the shape of the PDOS (see top of figure 6(b)) depends on the defect amount: type 1 corresponds to a low PDOS intensity whereas type 2 corresponds to a high number of defects. This is also true for

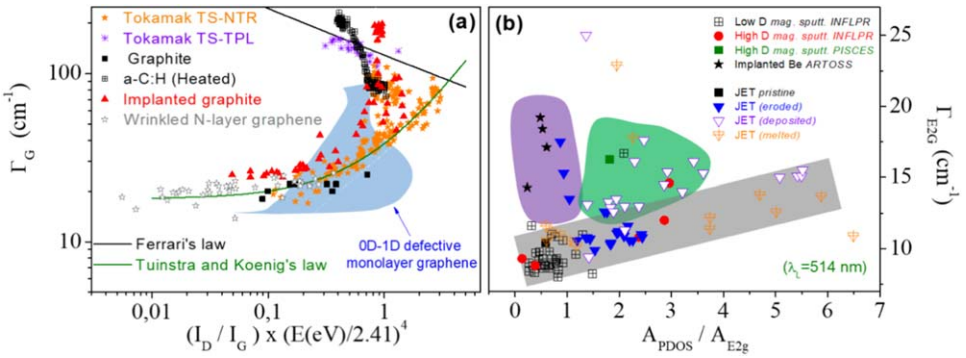

Figure 8. Defectivity behavior. (a) For carbon: G band width versus D over G band intensity ratio, whatever the laser wavelength [47, 70, 76–80]. (b) For beryllium: E_{2g} band width versus PDOS over E_{2G} intensity ratio, for 514 nm laser [6, 68]. Note that for figure (a) the intensity ratio is multiplied by a factor depending on the wavelength of the laser used to allow comparison with different lasers. This has not yet been studied in detail for beryllium. Also note that in figure (a) intensity is the height of the band whereas in figure (b) this is the area under the curve.

the shape of the $2E_{2G}$, $E_{2G}+B_{1G}$ and $2B_{1G}$ bands: they are broader for type 2 than for type 1, suggesting that they could be used to better estimate the amount or the type of defects in the material. What is missing up to now is a better characterization of the nature and amount of these defects with other techniques.

Another possible development in the future is related to the origin of the 2PDOS. Why the broad 2PDOS can be so intense for samples that contain only Be is not yet been understood. Comparing reflectivity measurements and Raman microscopy for 4 samples has revealed that there could be a link with porosity but this needs to be investigated in more details, e.g. by analysing thin foil samples where the porosity fingerprint becomes more important. The origin of the 2PDOS broad signature could be explained by the presence of native oxides. Reflectivity and XPS measurements tend to suggest that native oxides are not very thick (lower than 5 nm). However, there are no clear spectroscopic database of Raman signatures for Be native oxides to conclude native oxides are at the origin of the 2DPOS signature. Moreover, visible laser wavelengths used to perform Raman microscopy penetrate only about 20–40 nm in Be: depending on the unknown Raman cross section of this native oxide, 5 nm could be not so negligible. The only literature found so far on beryllium oxides reports PDOS or Raman frequencies of wurtzite BeO lying mainly in the range 650–750 cm^{-1} [61], or PDOS of a more exotic BeO_2 phase that could introduce modes with wavenumbers as high as 1125 cm^{-1} [62]. More BeO_x reference samples containing different stoichiometries and crystallographic phases are then needed to get reliable conclusions. The presence of beryllium deuteride is also something not yet established. In most publications, only frequencies of the hydride isotope are provided, that has to be multiplied by a correction factor taking into account a reduced mass involving deuterium (see details in [68]). Spectroscopic signatures are supposed to be lower than 1500 cm^{-1} for bulk phases, as shown by their PDOS [63–65]. Crystalline phases have been studied at ambient and high pressure environments, leading to a large number of bands below 1500 cm^{-1} [66]. We have also reported these bands, plus a doublet at higher wavenumber interpreted as surface sites, subsequently to the implantation of Be by 2 keV D ions with fluence in the range 2–4 10^{17} $D.cm^{-2}$ [90]. Amorphous beryllium deuteride is supposed to display a broad signature close to 1000 cm^{-1} according to the literature [67, 92]. This is, unfortunately, in the range where the 2PDOS lies. Using magnetron sputtering, and creating samples with a D content as high as 20 at.%, we have found that a broad signature could lie close to 1000 cm^{-1}, in agreement with previous references plus a narrower band close to 1200 cm^{-1} [68]. These two bands have been seen only on a very limited number of samples [68]. We believe that this is due to four reasons: (1) they fall at the same position as the intense 2PDOS signature. (2) Raman cross section of deuterides is low (divided by ≈10–100 to the intensities related to Be in figure 2). (3) Thermal stability of these deuterides limits the laser power we can use to acquire a spectrum in a reasonable time. (4) The maximum power that can be used is not exactly known as it depends on the structure of the material, and it takes extra time: you have to spend 2 −10 more time for only one sample to estimate experimentally the maximum power that should be used. For point (4), one can have an idea by looking on another material that is easier to work with in [45].

3.5. Spectroscopic parameter plots useful for nuclear fusion science

Below, we will detail useful points for fusion related samples. Briefly: these plots deliver an information about structure and the dispersion. It allows to distinguish zones were materials have been more exposed, heated,… Indirect information such as hydrogen content could also be deduced.

In more details, now, large amount of data for different samples can be extracted from fusion devices from the post mortem campaigns. Raman microscopy measurements, used to identify chemical bonds, could also

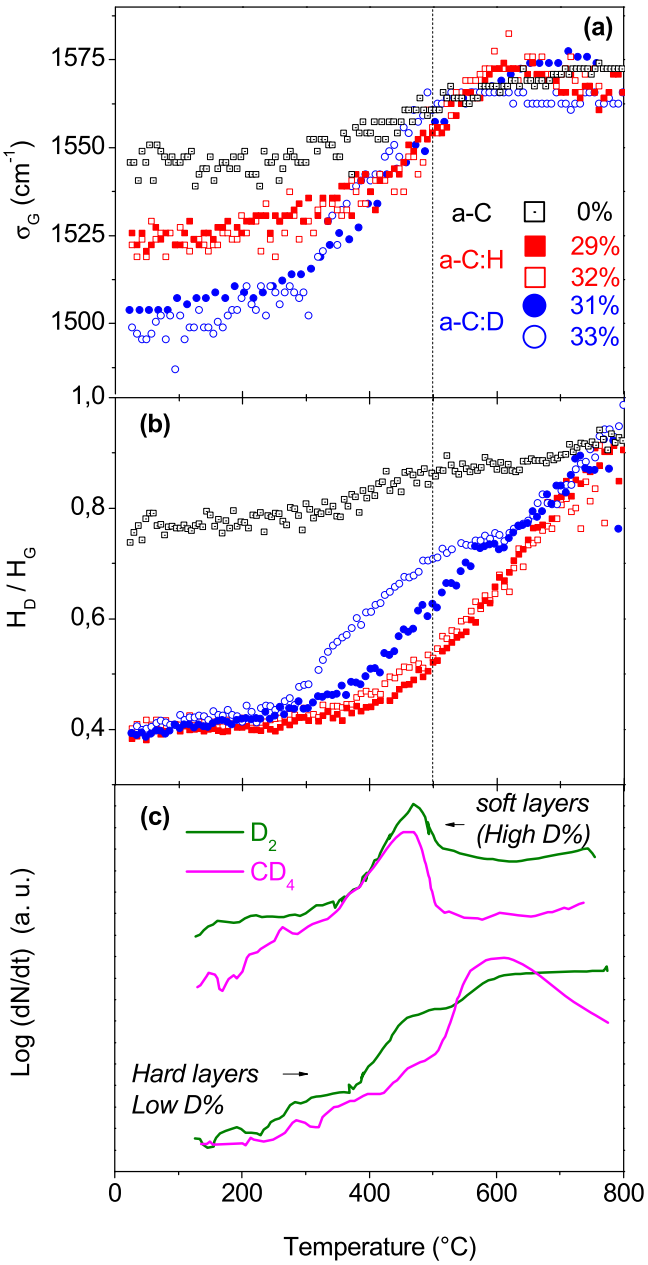

Figure 9. Band position and relative intensity ratio for amorphous hydrogenated and deuterated carbons. (a) G band position (carbon stretching). (b) D over G band intensity ratio. (c) Thermal desorption spectra of soft and hard samples. Data of figure (a) and (b) are from [81]. Data of figure (c) are from [82]. Laser wavelength used was 514 nm.

allow to investigate spatial erosion/deposition inhomogeneities on the plasma facing components from the micron scale (see the maps in figure 2) to the scale of the machine. Plotting some useful spectroscopic parameters together helps to capture quickly and self consistently those multiscale heterogeneity. Figure 7 displays the position of a typical Raman band as a function of its width for samples from fusion devices compared to well-characterized reference samples (not exposed to plasma). Both the band position and width have been normalized by their crystalline values to allow comparing different materials. For carbon (figure 7(a)), the plot focuses on the G band while for Be (figure 7(b)), the plot focuses on the band related to the E_{2G} mode. In the case of tungsten oxide (figure 7(c)), the band at 800 cm^{-1} is considered. Crystalline samples are close to the point of coordinate (1,1). For carbon, nanocrystalline graphite is detected at a band position close to 1 and a relative width multiplied by a factor 7 to 8. For higher widths, the material becomes amorphous. Depending on the structure of the carbon skeleton (related to the sp^2/sp^3 ratio) the amorphous carbons have different positions at the plot (it could be labelled ta-C:H, t-a:C, a-C:H,… depending on the structure, see details in [47]). In figure 7(a), the spreading of reference amorphous materials is due to the heat treatment that changes the structure by locally organizing it. The relative width value can be as high as 15–20. Samples collected from the Tore Supra tokamak [44, 69, 70] were measured to be amorphous on the toroidal pumped limiter which was

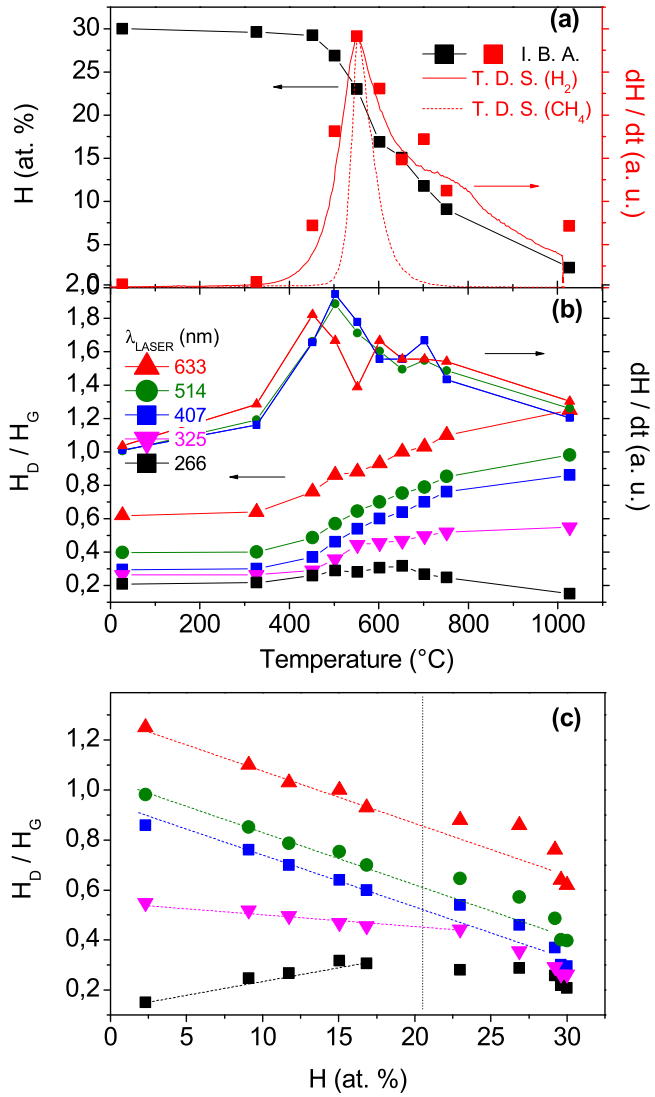

Figure 10. Hydrogen content evolution under post deposition heat treatment. (a) Ion beam and TDS. (b) D over G band relative intensity ratio evolution and its derivative with temperature. (c) H_D/H_G and H content correlation. Data of figure (a) is from [58]. Data of figures (b), (c) is from [48].

actively cooled [71, 72], and nanocrystalline on neutralizers that were not actively cooled. These observations contributed to conclusion that most of the deuterium trapped in the walls was not trapped on the neutralizers, that were heated close to 1000 °C (as deduced from the shape of the Raman spectra confirming temperature was high during operation) but on some regions of the limiter. Recent results on the stellarator W7-X revealed the presence of deuterated amorphous carbons with similar dispersion in the σ Vs Γ plot, as the one found on the Tore Supra limiter [31]. For beryllium, the trends are different: all data, regardless if they come from the JET tokamak or are reference materials synthetized in laboratory [49, 68, 73, 74] [6], are localized in roughly the same region of the band position with respect to the band width. Only eroded tiles from JET display a statistically relevant blue shift of the band position. However, this difference remains small compared to what is observed in case of carbon. The difference in behavior between Be and C could be explained because of the nature of the Raman signature in amorphous carbon: it is due to resonance effects [47], whereas there is no such effect for Be. Indeed, the increase of disorder in Be does not lead to a broad amorphous band which is a modification of the crystalline Raman allowed bands but to the rise of the PDOS. Broadening of the PDOS with the increase of defects (as shown in figure 6(b)) could be exploited in the future to retrieve information equivalent to the one retrieved exploiting spectroscopic information in the Raman spectra of amorphous carbon. Coupling XRD measurements with a refined fitting analysis of defective and highly defective Be spectra could change this lack of information in the future. For tungsten oxides (figure 7(c)), there are less data reported yet. WO_3 samples grown from a W polycrystalline material in an O_2 atmosphere and heated at different temperatures, or heated in air under laser irradiation show that band position is the same but the width has increased by a factor up to $\approx$10.

Erosion [50] or amorphization [75] both broaden the spectra by a factor of ≈10, but lead respectively to band blue shift of redshift, with the same amplitude (i.e. ≈ 4%). Such a high value for the blue shift has never been observed neither for Be nor for C. It has to be explained. Studying systematically the influence of disorder on a given phase is then required. However, the range of all possibilities, as illustrated by the richness of the spectra in figure 5(a), may induce some complexity in this kind of graph with many overlaps from the different phases. To put it in a nutshell, for carbons, plotting band position in function of band width allows to quickly view if tokamak samples studied are highly defective and could contain hydrogen isotopes. This is a qualitative information but it allows to compare different kind of tokamak zones and the big advantage is statistics could be made quickly. For beryllium, more information related to hydrogen content and defectivity will have to be extracted from the PDOS signal figure 7(b) display a poor variation. For tungsten oxide, results sound promising but a complete study focused on all the different kind of tungsten oxide spectral signatures will have to be performed in order to give refined usable plots.

Figure 8 displays the influence of defects on other parameters extracted from the spectra for C and Be. For carbon, the behaviour is well studied since decades while for Be the database is much scarcer. A similar graph for W oxides is beyond the scope of the present overview and requires more systematic studies in the future to observe trends similar to C and Be. A similar analysis for amorphous carbons containing hydrogen isotopes is shown in figure 9. For carbon (figure 8(a)), the D band relative intensity, coupled to the G band width is used as a way to estimate the number of defects. The dependence on the laser wavelength (illustrated in figure 3(b)) is well known and can be described by an appropriate numerical factor [76, 77, 93, 94]. Several laws, linking the characteristic scales and spectroscopic data, are successfully used to interpret the spectra to retrieve efficiently the relevant information. The nature of defects in graphene could be investigated for example, allowing to recognize punctual (0D) or linear (1D) defects [76]. Coupling ion bombardment, STM and Raman allowed to interpret the spectra of monolayer graphene [95]. Coupling XRD and Raman allowed to interpret the spectra of complex carbons [96]. In brief, there are two domains with two kinds of law [47]: first for amorphous carbon close or higher than $\Gamma_G = 80–100\ cm^{-1}$ [78–80], second for nanocrystalline carbon below this value [70, 76, 77, 93, 94], with phonon confinement [97] or local strain [98] that could modify band shapes. It should be noted that Γ_G and G band position evolve linearly for nanocrystalline carbon [70, 77]. Raman spectroscopy allows having access to these two kind of disorders. Although it was found recently that the D over G band intensity ratio might vary in a different way in some graphene folded systems [99, 100], highlighting the fact that a defect is not necessarily a well-defined concept. Studies are less active in researching beryllium then carbon. However, some trends could be reported in the Raman spectra. Plotting the band width of the Be allowed band in function of the PDOS relative intensity ratio (figure 8(b)) allows to reveal roughly three behaviors: a more or less linear relation, like the one labelled Tuinstra and Koenig's law in figure 8(a), a vertical region that correspond to implanted and some eroded berylliums, and an intermediate region. For Be, this plot is difficult to interpret up to now because of the lack of systematic reference samples obtained by varying temperature, fluence ion energy,… More systematic approach is needed to go a step further in interpreting tokamak data. Here we could say unambiguously that samples dominated by implantation effects are spread in the vertical region of figure 8(b). Further we focus on the relative intensity ratio of hydrogenated amorphous carbons and how we can derive hydrogen content with only this spectroscopic parameter.

4. Perspectives for H behavior with Raman in Be and WO: what we learned with carbon?

Retrieving the H content in hydrogenated amorphous carbon samples was investigated by means of Raman microscopy since a long time, by comparing for example the G band intensity and the slope of a photoluminescence background [101, 102]. Spectroscopic parameters sensitive to all kinds of bonded hydrogen are described in [58]. The G band intensity compared to the slope of a photoluminescence background was found to be sensitive to only one of the trapping sites. Figure 9 displays the evolution of the G band position and D over G band intensity as a function of temperature for 5 samples: one a-C (without D or H), two with D content initially containing 31 and 33 at.% and two with H content initially containing 29 and 32 at.% [81]. Measurements are made *in situ* and temperature is linearly increased at a typical 3 $Kmin^{-1}$ rate (environmental cell details, with a 1 bar Ar atmosphere, could be found in [81]). They are compared in figure 9(c) with thermal desorption spectra of typical hydrogen rich and hydrogen poor carbons [82], called respectively soft and hard layers [103]. The way H_D/H_G is related to the hydrogen content can be found in [58]. TDS shows that the more hydrogen the sample contains, the less stable it is: soft layers release H at a lower temperatures than hard layers. This behavior is not observed from the G band evolution with T but from the D over G band intensity ratios. In more details, the G band position increases when T increases for all samples, all D samples are grouped and placed below the H samples which are positioned below the a-C sample. This is because the reduced mass is

different between C-H and C-D. H or D indirect sensitivity could be probed up to 500 °C. For higher temperatures, all the data are grouped and evolve together with T, meaning there is no more indirect sensitivity to C-H or C-D bond, carbon skeleton frequency being the dominant one. For H_D/H_G situation is different: each sample behaves differently up to 700 °C. For samples containing more H or D, H_D/H_G starts to vary at a lower temperature than for the samples containing less H or D. All these observations demonstrate that H_D/H_G is sensitive to H or D release. Figure 10 demonstrates that H_D/H_G is not only sensitive but evolves linearly with the H or D content, which could be directly used to probe the H or D content in the material.

Figure 10(a) displays the H content evolution of the 29 at. % a-C:H sample, derived by ion beam analysis [58] and presented in figure 9. Two peaks are present corresponding to bond breaking of $C(sp^3)$-H and $C(sp^2)$-H bonds, separated by 200 °C . It also displays thermal desorption spectra of H_2 and CH_4. Deriving ion beam analysis and Raman signal as a function of temperature is of interest (figure 10(a)). Deriving the H content obtained by ion beam analysis also leads to two peaks. Deriving all the Raman parameters displays only the peak at low except H_D/H_G [58]. In figure 10(b), H_D/H_G is plotted for wavelengths from 266 to 633 nm. H_D/H_G increases the same way with temperature for visible wavelength, but differently for UV, due to a G band cross section that evolves differently in the UV [104]. This difference in behavior between the UV (266–325 nm) and visible ranges is also displayed in figure 10(c): H_D/H_G plotted as a function of the H content is linear for $\lambda_L = 488$ to 633 nm but not for 325 or 266 nm. Then, only the visible range can be used to easily derive the H content. We show this in figure 10(b): one can see two peaks, proving that not only H_D/H_G is sensitive to H coming from $C(sp^3)$-H bond splitting but also from $C(sp^2)$-H splitting. Figure 11 evidences the slow deuterium release during backing. Figure 11(a) was made in the framework of a post-mortem analyses in the Tore Supra tokamak. It has been shwon that: (1) there is a lack of deuterium in deposits whereas close to the surface (i.e. uppermost deposits) the D content could be close to 20 at.%, (2) a long term mechanism releasing D coming from larger depths occurs on long time scales [105, 106]. Raman microscopy measurements have been made *in situ* in heating cells (described above) on both laboratory samples and tokamak samples by performing long time scale isotherms [81, 107]. Laboratory samples are biased plasma enhanced chemically vapor deposited samples [58, 107]. Long term H release has also been observed by noticing the H_D/H_G slow increase. D content decrease with time displayed in figure 11(b) is calculated using the H_D/H_G measurement and the linear relation presented in figure 10(c). A refined analysis coupling multiwavelength Raman microscopy, TEM and EELS measurements has revealed that the oxygen content was found higher for longer heating times (1000 min at 500 °C leads to ≈5 at.%, whereas we reach ≈14 at. % waiting 2500 min) [48], see figure 11(c). This suggests that residual oxygen could form H_2O and lead to the H release on long time scales at low temperatures. Such analyses, and observations, do not yet exist for Be or W based materials. TEM measurements were done on cross sections to give access to the profile presented in figure 11(c). Raman measurements where done from the top and are averaged values of this depth profile as the spatial resolution is higher than the thickness of the layer probed (200 nm).

The methodology followed to study hydrogen behavior in carbon with Raman microscopy could be done for beryllium or tungsten oxides to go a step further. However, safety issues could limit studies made on Be. Another limitation is the low Raman cross section of beryllium and hydrides. For tungsten oxides, a systematic study could be very long thanks to the existence of the many phases.

5. Perspectives in the detection of boron based materials using Raman

Variations of structures involving boron seem to be as rich as the Magneli phases found in tungsten oxides. This is mainly because of the presence of boron icosahedral [108]. Figure 12 displays some of the most relevant spectra found in the literature, to help identifying future phases involving solid B in fusion related devices. Amorphous boron lies in the range 200–1200 cm^{-1} [109, 110] α, β and γ phases of boron are located below 1200 cm^{-1}, with mainly a 787 cm^{-1} and a 920 cm^{-1} band for α-B, the other phases being more rich [111]. Detecting the presence of amorphous boron deposited on oxidized W walls (which could be expected after boronization), as the frequencies of both tungsten oxide and amorphous boron are close, is rather challenging task. Therefore it is needed to use at least two laser wavelengths to change the ratio of bands coming from tungsten oxide and a-B phases.

Boron carbide exists in several phases, and stoichiometries. Not all have yet an identified Raman spectrum. The Raman spectrum of the B_4C phase, or close to this stoichiometry, which is carbon rich, is still debated, with the presence of some defects that play a role close to 1000 cm^{-1} [112], with a broad and intense band close to 1100cm^{-1}. The corresponding PDOS exhibits modes below 1200 cm^{-1} plus modes localized close to 1600 cm^{-1}, that could be confused, or hidden by impurities of sp^2 carbons. Amorphous B_4C leads to highly intense extra bands at 1330 and 1810 cm^{-1} [113].

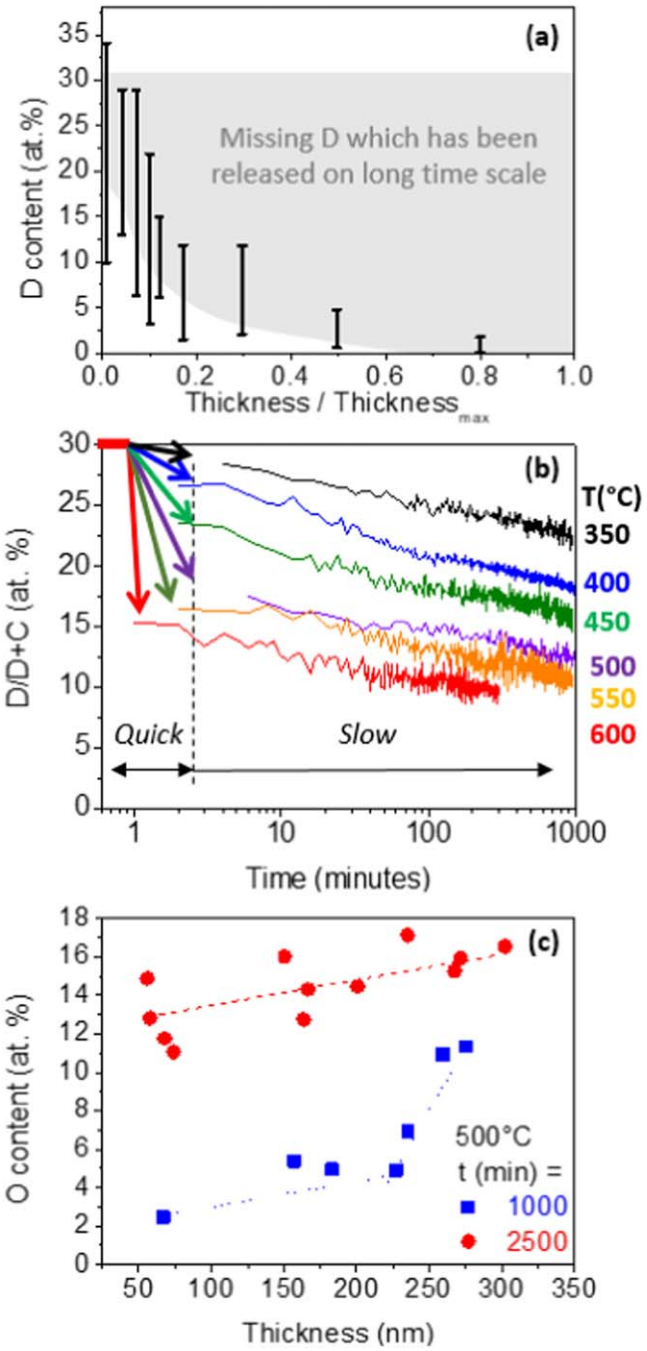

Figure 11. Slow deuterium release during backing. (a) D content decrease in Tore Supra deposits, adapted from [105, 106]. (b) D content evolution deduced from the Raman spectra in laboratory samples. (c) In depth oxygen content evolution at 500 °C with various heating time for a laboratory sample. Data of figure (a) are from [105, 106]. Data of figure (b) are from [81, 107]. Data of figure (c) are from [48].

Boron oxides exist in several forms. B_2O_3 is a glass (network of connected planar BO_3 triangles). Corresponding Raman spectra display a strong and sharp band at 808 cm^{-1}, accompanied by weaker bands close to 500 and 1250 cm^{-1} [114]. Amorphous B_2O_3 spectrum is calculated to be composed of 4 broad overlapping bands at 130, 670, 945 and 1174 cm^{-1} [115]. Amorphous B_2O_3 and tungsten oxide could be disentangled mainly because of the spectral range of a-B_2O_3 which is larger than the one of tungsten oxides. One boron suboxide, B_6O, with peculiar properties is also reported [116]. Its spectrum is close to the one of a-B_2O_3 but with different intensity ratio. In figure 12(b), we present a spectrum recorded close to the WEST divertor. This spectrum is compared with a typical spectra presented earlier. It can be seen that it looks like the spectrum of an amorphous boron. We also display a spectrum recorded at a higher laser power. The spectrum displays two extra narrow bands which could be due to crystalline B_2O_3, created by temperature increase of the amorphous material under the laser beam.

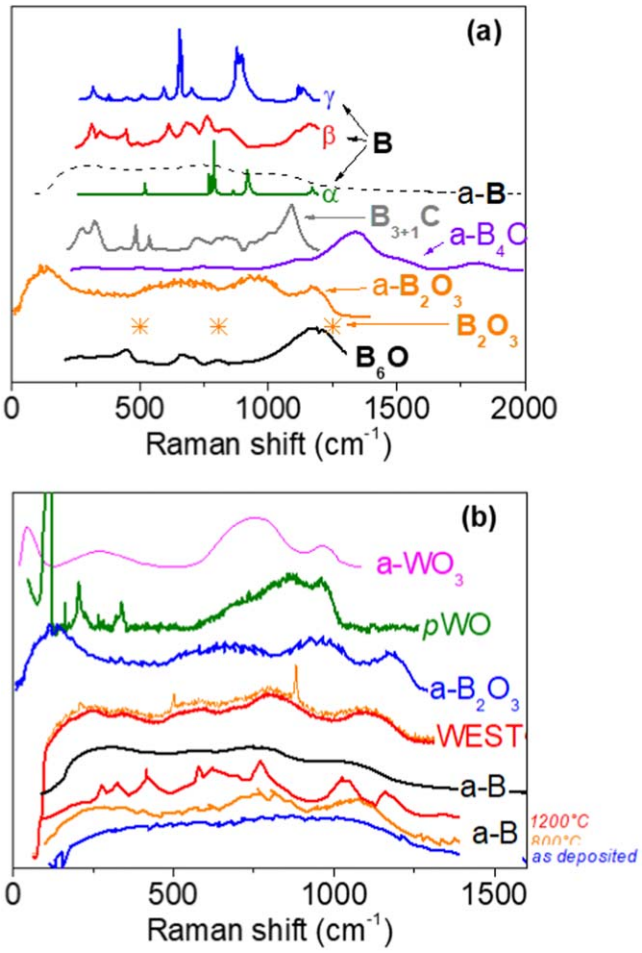

Figure 12. Boron based Raman spectra useful to detect how boron is bonded after boronization. (a) Literature survey of B related materials. (b) Comparison of a deposit with relevant B related materials and tungsten oxides. Data origins are described in the text. As deposited, 800 °C and 1200 °C correspond to post heat treatment of a-B from [109]. Laser wavelength used for WEST measurements is 514 nm but 633 nm give the same spectra.

6. Conclusions

We have presented the state-of-the-art use of Raman microscopy to characterize materials involved in nuclear fusion PFCs. We have also given guidelines on the use of this technique. Basing our approach on what we learned during the tokamak carbon era, we have presented what it is possible to do by characterizing machine samples alone (i.e. without comparing to reference samples). We have also shown what we gain by studying well-characterized laboratory samples. As an example, by systematic characterizations of laboratory synthesized amorphous C samples, it was possible, from Raman spectra, to retrieve the H content and the way H was bonded to C in tokamak samples. This allowed to efficiently and quantitatively contribute to the H isotope inventory in nuclear fusion devices. Moreover, in the case of Tore Supra deposits, it was possible to highlight the driving role of O contamination in the long-term D release, leading to a diminution of the in-depth D content on long time-scale during baking operations. Obtaining such information, not merely on retention amounts but on retention mechanisms, could be in principle achievable by a similar approach with plasma facing materials containing beryllium or tungsten oxides. We have shown that the presence of oxides, hydrides, defects… can be detected because chemical bonds are modified of created in the material. Finally, we have discussed the possibility to identify boron-rich phases, as they could be observed in some devices due to boronization. Notably, we report the first identification of amorphous boron deposits in the WEST tokamak by means of Raman microscopy. This last result shows that Raman microscopy will be an efficient tool to detect how boron binds with the various elements present in nuclear fusion plasma facing components.

Acknowledgments

This work has been carried out within the framework of the EUROfusion Consortium, funded by the European Union via the Euratom Research and Training Programme (Grant Agreement No 101052200 EUROfusion).

Views and opinions expressed are however those of the author(s) only and do not necessarily reflect those of the European Union or the European Commission. Neither the European Union nor the European Commission can be held responsible for them.

Data availability statement

There are too many meta data to be shared in a convenient way. Personnal requests allow to transmit useful information efficiently. The data that support the findings of this study are available upon reasonable request from the authors.

Conflicts of interest

The authors declare no conflict of interest. The authors declare that they have no known competing financial interests or personal relationships that could have appeared to influence the work reported in this paper

ORCID iDs

C Pardanaud https://orcid.org/0000-0001-8974-4396
C Martin https://orcid.org/0000-0002-4704-3273
D Dellasega https://orcid.org/0000-0002-7389-9307
M Passoni https://orcid.org/0000-0002-7844-3691
C Porosnicu https://orcid.org/0000-0003-0561-0644

References

[1] Pitts R A *et al* 2019 Physics basis for the first ITER tungsten divertor *Nuclear Materials and Energy* **20** 100696
[2] Matthews G F *et al* 2011 JET ITER-like wall-overview and experimental programme *Phys. Scr.* **T145** 014001
[3] Vassallo E, Angella G, Caniello R, Deambrosis S, Inzoli F, Miorin E and Pedroni M 2015 Effects of nitrogen concentration on microstructure of tungsten coatings synthesized by plasma sputtering method *J. Fusion Energy* **34** 1246–51
[4] Linke J, Du J, Loewenhoff T, Pintsuk G, Spilker B, Steudel I and Wirtz M 2019 Challenges for plasma-facing components in nuclear fusion *Matter Radiat. Extremes* **4** 056201
[5] Pitts R A *et al* 2013 A full tungsten divertor for ITER: physics issues and design status *J. Nucl. Mater.* **438** S48–56
[6] Kumar M *et al* 2018 Identification of BeO and BeOxDy in melted zones of the JET Be limiter tiles: Raman study using comparison with laboratory samples *Nuclear Materials and Energy* **17** 295–301
[7] Makepeace C *et al* 2019 The effect of beryllium oxide on retention in JET ITER-like wall tiles *Nuclear Materials and Energy* **19** 346–51
[8] Dibon M, Rohde V, Stelzer F, Hegele K, Uhlmann M and Team A U 2021 New boronization system at ASDEX upgrade *Fusion Eng. Des.* **165** 112233
[9] Bortolon A *et al* 2019 Real-time wall conditioning by controlled injection of boron and boron nitride powder in full tungsten wall ASDEX Upgrade *Nuclear Materials and Energy* **19** 384–9
[10] Brezinsek S *et al* 2017 Plasma-wall interaction studies within the EUROfusion consortium: progress on plasma-facing components development and qualification *Nuclear Fusion* **57** 384–9
[11] Mayer M *et al* 2017 Erosion and deposition in the JET divertor during the second ITER-like wall campaign *Phys. Scr.* **T170** 014058
[12] Greuner H, Maier H, Balden M, Linsmeier C, Boswirth B, Lindig S, Norajitra P, Antusch S and Rieth M 2013 Investigation of european tungsten materials exposed to high heat flux H/He neutral beams *J. Nucl. Mater.* **442** S256–60
[13] Arnoux G *et al* 2014 Power handling of the JET ITER-like wall *Phys. Scr.* **T159** 014009
[14] Brezinsek S *et al* 2015 Beryllium migration in JET ITER-like wall plasmas *Nucl. Fusion* **55** 063021
[15] Bykov I *et al* 2016 Studies of Be migration in the JET tokamak using AMS with Be-10 marker *Nuclear Instruments & Methods in Physics Research section B-Beam Interactions with Materials and Atoms* **371** 370–5
[16] Fortuna-Zalesna E, Grzonka J, Moon S, Rubel M, Petersson P, Widdowson A and Contributors J E T 2017 Fine metal dust particles on the wall probes from JET-ILW *Phys. Scr.* **T170** 014038
[17] Fortuna-Zalesna E, Grzonka J, Rubel M, Garcia-Carrasco A, Widdowson A, Baron-Wiechec A, Ciupinski L and Contributors J E T 2017 Studies of dust from JET with the ITER-like wall: composition and internal structure *Nuclear Materials and Energy* **12** 582–7
[18] Masuzakil S *et al* 2017 Analyses of microstructure, composition and retention of hydrogen isotopes in divertor tiles of JET with the ITER-like wall *Phys. Scr.* **T170** 014031
[19] Heinola K, Widdowson A, Likonen J, Alves E, Baron-Wiechec A, Barradas N, Brezinsek S, Catarino N, Coad P and Koivuranta S 2016 Long-term fuel retention in JET ITER-like wall *Phys. Scr.* **T167** 014075
[20] Likonen J *et al* 2016 Deuterium trapping and release in JET ITER-like wall divertor tiles *Phys. Scr.* **T167** 014074
[21] Bernard E *et al* 2019 Tritium retention in W plasma-facing materials: Impact of the material structure and helium irradiation *Nuclear Materials and Energy* **19** 403–10
[22] Kreter A, Brandt C, Huber A, Kraus S, Moller S, Reinhart M, Schweer B, Sergienko G and Unterberg B 2015 Linear plasma device psi-2 for plasma-material interaction studies *Fusion Sci. Technol.* **68** 8–14
[23] Linsmeier C, Unterberg B, Coenen J W, Doerner R P, Greuner H, Kreter A, Linke J and Maier H 2017 Material testing facilities and programs for plasma-facing component testing *Nucl. Fusion* **57** 092012
[24] Sala M, Uccello A, Dellasega D, Pedroni M, Vassallo E and Passoni M 2020 Exposures of bulk W and nanostructured W coatings to medium flux D plasmas *Nuclear Materials and Energy* **24** 100779

[25] Uccello A et al 2020 Effects of a nitrogen seeded plasma on nanostructured tungsten films having fusion-relevant features Nuclear Materials and Energy 25 100808
[26] Paris P, Jogi I, Piip K, Passoni M, Dellasega D, Grigore E, Arnoldbik W M and van der Meiden H 2021 In-situ LIBS and NRA deuterium retention study in porous W-O and compact W coatings loaded by Magnum-PSI Fusion Eng. Des. 168 112403
[27] Brezinsek S and Contributors J-E 2015 Plasma-surface interaction in the Be/W environment: Conclusions drawn from the JET-ILW for ITER J. Nucl. Mater. 463 11–21
[28] Brezinsek S et al 2019 Erosion, screening, and migration of tungsten in the JET divertor Nucl. Fusion 59 096035
[29] Balden M et al 2021 Erosion and redeposition patterns on entire erosion marker tiles after exposure in the first operation phase of WEST Phys. Scr. 96 124020
[30] Martin C et al 2021 First post-mortem analysis of deposits collected on ITER-like components in WEST after the C3 and C4 campaigns Phys. Scr. 96 124035
[31] Dhard C P et al 2021 Plasma-wall interaction studies in W7-X: main results from the recent divertor operations Phys. Scr. 96 124059
[32] Hakola A et al 2021 Gross and net erosion balance of plasma-facing materials in full-W tokamaks Nucl. Fusion 61 116006
[33] Weckmann A, Petersson P, Kirschner A, Wienhold P, Brezinsek S, Kreter A, Pospieszczyk A and Rubel M 2017 Whole-machine material migration studies in the TEXTOR tokamak with molybdenum Nuclear Materials and Energy 12 518–23
[34] Weckmann A et al 2018 Review on global migration, fuel retention and modelling after TEXTOR decommission Nuclear Materials and Energy 17 83–112
[35] Pelicon P et al 2011 Fuel retention study in fusion reactor walls by micro-NRA deuterium mapping Nuclear Instruments & Methods in Physics Research section B-Beam Interactions with Materials and Atoms 269 2317–21
[36] Alves L C, Alves E, Barradas N P, Mateus R, Carvalho P, Coad J P, Widdowson A M, Likonen J and Koivuranta S 2010 Erosion and re-deposition processes in JET tiles studied with ion beams Nuclear Instruments & Methods in Physics Research section B-Beam Interactions with Materials and Atoms 268 1991–6
[37] Martin C, Pegourie B, Ruffe R, Marandet Y, Giacometti G, Pardanaud C, Languille P, Panayotis S, Tsitrone E and Roubin P 2011 Structural analysis of eroded carbon fiber composite tiles of Tore Supra: insights on ion transport and erosion parameters Phys. Scr. T145 4
[38] Mellet N et al 2014 Modelling of the micrometric erosion pattern observed on the Tore Supra limiter tiles Nucl. Fusion 54 123006
[39] Guterl J, Smirnov R D, Krasheninnikov S I, Zibrov M and Pisarev A A 2015 Theoretical analysis of deuterium retention in tungsten plasma-facing components induced by various traps via thermal desorption spectroscopy Nucl. Fusion 55 093017
[40] Hodille E A, Ferro Y, Fernandez N, Becquart C S, Angot T, Layet J M, Bisson R and Grisolia C 2016 Study of hydrogen isotopes behavior in tungsten by a multi trapping macroscopic rate equation model Phys. Scr. T167 014011
[41] Pagnier T, Boulova M, Sergent N, Bouvier P and Lucazeau G 2007 Nanopowders and nanostructured oxides: phase transitions and surface reactivity J. Raman Spectrosc. 38 756–61
[42] Kremer K, Schwarz-Selinger T and Jacob W 2021 Influence of thin tungsten oxide films on hydrogen isotope uptake and retention in tungsten-Evidence for permeation barrier effect Nuclear Materials and Energy 27 100991
[43] Stankevich V G, Svechnikov N Y and Kolbasov B N 2023 Comparative analysis of spectroscopic studies of tungsten and carbon deposits on plasma-facing components in thermonuclear fusion reactors Symmetry 15 623
[44] pardanaud C, Martin C and Roubin P 2017 Raman microscopy: a suitable tool for characterizing surfaces in interaction with plasmas in the field of nuclear fusion Raman Spectroscopy and Applications ed K Maaz (InTech) 3–30
[45] Pardanaud C et al 2020 Post-mortem analysis of tungsten plasma facing components in tokamaks: Raman microscopy measurements on compact, porous oxide and nitride films and nanoparticles Nucl. Fusion 60 086004
[46] Pardanaud C, Areou E, Martin C, Ruffe R, Angot T, Roubin P, Hopf C, Schwarz-Selinger T and Jacob W 2012 Raman micro-spectroscopy as a tool to measure the absorption coefficient and the erosion rate of hydrogenated amorphous carbon films heat-treated under hydrogen bombardment Diamond Relat. Mater. 22 92–5
[47] Merlen A, Buijnsters J G and Pardanaud C 2017 A guide to and review of the use of multiwavelength raman spectroscopy for characterizing defective aromatic carbon solids: from graphene to amorphous carbons Coatings 7 153
[48] Lajaunie L, Pardanaud C, Martin C, Puech P, Hu C, Biggs M J and Arenal R 2017 Advanced spectroscopic analyses on a:C-H materials: revisiting the EELS characterization and its coupling with multi-wavelength Raman spectroscopy Carbon 112 149–61
[49] Rusu M I et al 2017 Preparing the future post-mortem analysis of beryllium-based JET and ITER samples by multi-wavelengths Raman spectroscopy on implanted Be, and co-deposited Be Nucl. Fusion 57 076035
[50] Addab Y et al 2016 Formation of thin tungsten oxide layers: characterization and exposure to deuterium Phys. Scr. T167 014036
[51] Reich S and Thomsen C 2004 Raman spectroscopy of graphite Philosophical Transactions of the Royal Society a-Mathematical Physical and Engineering Sciences 362 2271–88
[52] Liang L B, Zhang J, Sumpter B G, Tan Q H, Tan P H and Meunier V 2017 Low-frequency shear and layer-breathing modes in raman scattering of two-dimensional materials Acs Nano 11 11777–802
[53] Lazzeri M, Piscanec S, Mauri F, Ferrari A C and Robertson J 2006 Phonon linewidths and electron-phonon coupling in graphite and nanotubes Phys. Rev.B 73 155426
[54] Cancado L G, Takai K, Enoki T, Endo M, Kim Y A, Mizusaki H, Speziali N L, Jorio A and Pimenta M A 2008 Measuring the degree of stacking order in graphite by Raman spectroscopy Carbon 46 272–5
[55] Ferrari A C et al 2006 Raman spectrum of graphene and graphene layers Phys. Rev. Lett. 97 187401
[56] kawashima Y and Katagari G 1999 Observation of the out-of-plane mode in the Raman scattering from the graphite edge plane Phy. Rev.B 59 62
[57] Pardanaud C, Cartry G, Lajaunie L, Arenal R and Buijnsters J G 2019 Investigating the possible origin of raman bands in defective sp(2)/sp(3) carbons below 900 cm(-1): phonon density of states or double resonance mechanism at play? C-Journal of Carbon Research 5 79
[58] Pardanaud C, Martin C, Roubin P, Giacometti G, Hopf C, Schwarz-Selinger T and Jacob W 2013 Raman spectroscopy investigation of the H content of heated hard amorphous carbon layers Diam. Relat. Mater. 34 100–4
[59] Pardanaud C, Martin C, Cartry G, Ahmad A, Schiesko L, Giacometti G, Carrere M and Roubin P 2015 In-plane and out-of-plane defects of graphite bombarded by H, D and He investigated by atomic force and Raman microscopies J. Raman Spectrosc. 46 256–65
[60] Hakola A et al 2020 Effect of composition and surface characteristics on fuel retention in beryllium-containing co-deposited layers Phys. Scr. T171 014038
[61] Malakkal L, Szpunar B, Siripurapu R K, Zuniga J C and Szpunar J A 2017 Thermal conductivity of wurtzite and zinc blende cubic phases of BeO from ab initio calculations Solid State Sci. 65 79–87
[62] Zhang S T, Li F, Xu H Y and Yang G C 2017 Pressure-induced stable beryllium peroxide Inorg. Chem. 56 5233–8

[63] An X Y, Zeng T X and Ren W Y 2017 Structural, electronic and optical properties of BeH2: A density functional theory study *Mater. Res. Express* **4** 036302
[64] Hector L G Jr, Herbst J F and Kresse G 2007 Ab Initio thermodynamic and elastic properties of alkaline-earth metals and their hydrides *Phys. Rev.*B **76** 014121
[65] Virot F, Ferry L, Ferro Y, Pardanaud C and Barrachin M 2017 Contribution to a better evaluation of the dust speciation in case of an accident in ITER *Fusion Eng. Des.* **124** 1171–6
[66] Pépin C and Loubeyre P 2016 Layered structure and re-entrant disproportionation observed in crystalline BeH2 under pressure *Phys. Rev.*B **93** 224104
[67] Wang X F and Andrews L 2005 Infrared spectra and structures of the coinage metal dihydroxide molecules *Inorg. Chem.* **44** 9076–83
[68] Pardanaud C *et al* 2021 D retention and material defects probed using Raman microscopy in JET limiter samples and beryllium-based synthesized samples *Phys. Scr.* **96** 124031
[69] Pardanaud C *et al* 2011 Raman study of CFC tiles extracted from the toroidal pump limiter of Tore Supra *J. Nucl. Mater.* **415** S254–7
[70] Pardanaud C, Martin C and Roubin P 2014 Multiwavelength Raman spectroscopy analysis of a large sampling of disordered carbons extracted from the Tore Supra tokamak *Vib. Spectrosc.* **70** 187–92
[71] Dittmar T *et al* 2009 Deuterium Inventory in Tore Supra: status of post-mortem analyses *Phys. Scr.* **T138** 014027
[72] Dittmar T *et al* 2011 Deuterium Inventory in Tore Supra (DITS): 2nd post-mortem analysis campaign and fuel retention in the gaps *J. Nucl. Mater.* **415** S757–60
[73] Pardanaud C *et al* 2016 Raman microscopy investigation of beryllium materials *Phys. Scr.* **T167** 014027
[74] Pardanaud C *et al* 2015 Hydrogen retention in beryllium: concentration effect and nanocrystalline growth *J. Phys. Condens. Matter* **27** 475401
[75] Boulova M and Lucazeau G 2002 Crystallite nanosize effect on the structural transitions of WO3 studied by Raman spectroscopy *J. Solid State Chem.* **167** 425–34
[76] Cancado L G, da Silva M G, Ferreira E H M, Hof F, Kampioti K, Huang K, Penicaud A, Achete C A, Capaz R B and Jorio A 2017 Disentangling contributions of point and line defects in the Raman spectra of graphene-related materials *2D Mater.* **4** 025039
[77] Cancado L G, Takai K, Enoki T, Endo M, Kim Y A, Mizusaki H, Jorio A, Coelho L N, Magalhaes-Paniago R and Pimenta M A 2006 General equation for the determination of the crystallite size L-a of nanographite by Raman spectroscopy *Appl. Phys. Lett.* **88** 163106
[78] Wagner J, Ramsteiner M, Wild C H and Koidl P 1989 Resonant Raman scattering of amorphous carbon and polycrystalline diamond films *Phys. Rev.* B **40** 1817–24
[79] Ferrari A C and Robertson J 2000 Interpretation of Raman spectra of disordered and amorphous carbon *Phys. Rev.* B **61** 14095–107
[80] Ferrari A C and Robertson J 2001 Resonant Raman spectroscopy of disordered, amorphous, and diamondlike carbon *Phys. Rev.*B **64** 075414
[81] Pardanaud C, Martin C, Giacometti G, Mellet N, Pegourie B and Roubin P 2015 Thermal stability and long term hydrogen/deuterium release from soft to hard amorphous carbon layers analyzed using in situ Raman spectroscopy. Comparison with tore supra deposits *Thin Solid Films* **581** 92–8
[82] Salançon E, Dürbeck T, Schwarz-Selinger T, Genoese F and Jacob W 2008 Redeposition of amorphous hydrogenated carbon films during thermal decomposition *J. Nucl. Mat.* **376** 160
[83] Addonizio M L, Castaldo A, Antonaia A, Gambale E and Iemmo L 2012 Influence of process parameters on properties of reactively sputtered tungsten nitride thin films *J. Vac. Sci. Technol.*A **30** 031506
[84] Zheng H D, Ou J Z, Strano M S, Kaner R B, Mitchell A and Kalantar-Zadeh K 2011 Nanostructured tungsten oxide - properties, synthesis, and applications *Adv. Funct. Mater.* **21** 2175–96
[85] Migas D B, Shaposhnikov V L and Borisenko V E 2010 Tungsten oxides. II. The metallic nature of Magneli phases *J. Appl. Phys.* **108** 093714
[86] Boulova M, Rosman N, Bouvier P and Lucazeau G 2002 High-pressure Raman study of microcrystalline WO3 tungsten oxide *Journal of Physics-Condensed Matter* **14** 5849–63
[87] Vargas-Consuelos C I, Seo K, Camacho-Lopez M and Graeve O A 2014 Correlation between particle size and raman vibrations in WO3 powders *J. Phys. Chem.* C **118** 9531–7
[88] Dellasega D, Merlo G, Conti C, Bottani C E and Passoni M 2012 Nanostructured and amorphous-like tungsten films grown by pulsed laser deposition *J. Appl. Phys.* **112** 084328
[89] Mateus R, Dellasega D, Passoni M, Siketic Z, Radovic I B, Hakola A and Alves E 2018 Helium load on W-O coatings grown by pulsed laser deposition *Surf. Coat. Technol.* **355** 215–21
[90] Pardanaud C, Addab Y, Martin C, Roubin P, Pegourié B, Oberkofler M, Köppen M, Dittmar T and Linsmeier C 2015 Raman microscopy as a defect microprobe for hydrogen bonding characterization in materials used in fusion applications *physica status solidi (c)* **12** 98–101
[91] Minissale M, De Canonville C L, Pardanaud C, Butoi B, Bisson R and Gallais L 2022 The role of defects, deuterium, and surface morphology on the optical response of beryllium *Nucl. Fusion* **62** 056012
[92] Sampath S, Kolesnikov A I, Lantzky K M and Yarger J L 2008 Vibrational dynamics of amorphous beryllium hydride and lithium beryllium hydrides *J. Chem. Phys.* **128** 134512
[93] Cancado L G, Jorio A, Martins Ferreira E H, Stavale F, Achete C A, Capaz R B, Moutinho M V O, Lombardo A, Kulmala T S and Ferrari A C 2011 Quantifying Defects in Graphene via Raman Spectroscopy at Different Excitation Energies *Nano Lett.* **11** 3190–6
[94] Cancado L G, Jorio A and Pimenta M A 2007 Measuring the absolute Raman cross section of nanographites as a function of laser energy and crystallite size *Phys. Rev.*B **76** 064304
[95] Lucchese M M, Stavale F, Ferreira E H M, Vilani C, Moutinho M V O, Capaz R B, Achete C A and Jorio A 2010 Quantifying ion-induced defects and Raman relaxation length in graphene *Carbon* **48** 1592–7
[96] Puech P, Kandara M, Paredes G, Moulin L, Weiss-Hortala E, Kundu A, Ratel-Ramond N, Plewa J M, Pellenq R and Monthioux M 2019 Analyzing the Raman Spectra of graphenic carbon materials from kerogens to nanotubes: what type of information can be extracted from defect bands? *C-Journal of Carbon Research* **5** 69
[97] Puech P, Plewa J M, Mallet-Ladeira P and Monthioux M 2016 Spatial confinement model applied to phonons in disordered graphene-based carbons *Carbon* **105** 275–81
[98] Lee J E, Ahn G, Shim J, Lee Y S and Ryu S 2012 Optical separation of mechanical strain from charge doping in graphene *Nat. Commun.* **3** 1024
[99] Picheau E *et al* 2021 Intense Raman D Band without disorder in flattened carbon nanotubes *Acs Nano* **15** 596–603
[100] Nikolaievskyi D *et al* 2023 Wrinkling and crumpling in twisted few and multilayer CVD graphene: High density of edge modes influencing Raman spectra *Carbon* **203** 650–60

[101] Buijnsters J G, Gago R, Jiménez I, Camero M, Agullo-Rueda F and Gomez-Aleixandre C 2009 Hydrogen quantification in hydrogenated amorphous carbon films by infrared, Raman, and x-ray absorption near edge spectroscopies *J. Appl. Phys.* **105** 093510
[102] Casiraghi C, Ferrari A C and Robertson J 2005 Raman spectroscopy of hydrogenated amorphous carbons *Phys. Rev.*B **72** 085401
[103] Jacob W and Moller W 1993 On the structure of thin hydrocarbon films *Appl. Phys. Lett.* **63** 1771–3
[104] Casiraghi C 2011 Effect of hydrogen on the UV Raman intensities of diamond-like carbon *Diam. Relat. Mater.* **20** 120–2
[105] Panayotis S, Pegourie B, Caprin E, Douai D, Hatchressian J C, Negrier V, Pascal J Y, Vartanian S, Bucalossi J and Monier-Garbet P 2013 Deuterium inventory in Tore Supra: Contribution of carbon deposits outgassing *J. Nucl. Mater.* **438** S1059–62
[106] Pegourie B *et al* 2013 Deuterium inventory in tore supra: coupled carbon-deuterium balance *J. Nucl. Mater.* **438** S120–5
[107] Pardanaud C, Martin C, Giacometti G, Roubin P, Pegourie B, Hopf C, Schwarz-Selinger T, Jacob W and Buijnsters J G 2013 Long-term H-release of hard and intermediate between hard and soft amorphous carbon evidenced by in situ Raman microscopy under isothermal heating *Diamond Relat. Mater.* **37** 92–6
[108] Werheit H *et al* 2010 Raman effect in icosahedral boron-rich solids *Sci. Technol. Adv. Mater.* **11** 023001
[109] Dellasega D, Russo V, Pezzoli A, Conti C, Lecis N, Besozzi E, Beghi M, Bottani C E and Passoni M 2017 Boron films produced by high energy Pulsed Laser Deposition *Mater. Des.* **134** 35–43
[110] Lannin J S 1978 Raman-scattering in amorphous boron *Solid State Commun.* **25** 363–6
[111] Parakhonskiy G, Dubrovinskaia N, Bykova E, Wirth R and Dubrovinsky L 2011 Experimental pressure-temperature phase diagram of boron: resolving the long-standing enigma *Sci. Rep.* **1** 96
[112] Roma G, Gillet K, Jay A, Vast N and Gutierrez G 2021 Understanding first-order Raman spectra of boron carbides across the homogeneity range *Phys. Rev. Mater.* **5** 063601
[113] Reddy K M, Liu P, Hirata A, Fujita T and Chen M W 2013 Atomic structure of amorphous shear bands in boron carbide *Nat. Commun.* **4** 2483
[114] Hassan A K, Torell L M, Borjesson L and Doweidar H 1992 Structural-changes of B2O3 through the liquid-glass transition range - a raman-scattering study *Phys. Rev.* B **45** 12797–805
[115] Sahu P, Pente A A, Singh M D, Chowdhri I A, Sharma K, Goswami M, Ai S M, Shenoy K T and Mohan S 2019 *Molecular dynamics simulation of amorphous SiO2, B2O3, Na2O-SiO2, Na2O-B2O3, and Na2O-B2O3-SiO2 glasses with variable compositions and with Cs2O and SrO dopants J. Phys. Chem.* B **123** 6290–302
[116] Wang Z W, Zhao Y S, Lazor P, Annersten H and Saxena S K 2005 In situ pressure Raman spectroscopy and mechanical stability of superhard boron suboxide *Appl. Phys. Lett.* **86** 041911